# Passive Behavior and Passivity Breakdown of AISI 304 in LiBr Solutions through Scanning Electrochemical Microscopy

**R. M. Fernandez-Domene, R. Sánchez-Tovar, and J. García-Antón[z]**

Ingeniería Electroquímica y Corrosión (IEC), Departamento de Ingeniería Química y Nuclear, ETSI Industriales, Universitat Politècnica de València, Camino de Vera s/n, 46022 Valencia, Spain

[z]E-mail: jgarciaa@iqn.upv.es

The passive behavior and passivity breakdown of AISI 304 stainless steel in LiBr solutions has been investigated by means of scanning electrochemical microscopy (SECM). The sample generation – tip collection (SG-TC) mode was used to operate the SECM and the tip potential was biased to detect the electroactive species. The evolution of the current at the ultramicroelectrode tip with the applied potential within the passive range was followed at different LiBr concentrations. Results show that the absolute value of the current at the tip increases with the applied potential. Additionally, SECM was also used to detect stable pits formed on the stainless steel surface in a 0.2 M LiBr solution. The results show clear evidence of the presence of high amounts of other reducible species (metal cations) apart from oxygen. Also, the dish-shape morphology of the pits observed using Confocal Laser Scanning Microscopy will be discussed in relation to the kinetics of the reactions observed using SECM.

Manuscript submitted April 22, 2014; revised manuscript received September 5, 2014.
Published xx xx, xxxx.

## 1. INTRODUCTION

Stainless steel (SS) is a generic name commonly used for the group of iron-based alloys which are the most widely known metallic materials [1-3]. One of the main characteristics of SS is their resistance to corrosion in many environments, which is provided by a very thin and protective surface oxide film, known as passive film. It is generally accepted that passive films formed on SS have a duplex structure which consists of an inner region rich in chromium and an outer region rich in iron [4-9]. Austenitic SS are the most common and familiar types of SS [2]. Among austenitic SS, type 304 SS contains approximately 18 wt. % of chromium and 8 wt. % of nickel and is widely used in chemical processing equipment, for food, dairy, and beverage industries, for heat exchangers and in the milder chemicals.

Pitting corrosion of passive metals is considered to be more dangerous than uniform corrosion, since it is more difficult to detect, predict and design against [10]. Localized breakdown of passive films leads to an enhancement of metal dissolution at the site of the pit due to the formation of a galvanic cell between the pit (anode) and the intact passive film (cathode). Therefore, pitting corrosion may result in perforation of a pipe or in structural failure [2].

Scanning Electrochemical Microscopy (SECM) has become a powerful technique for quantitative investigations of corrosion processes, including the study of pitting corrosion and other localized degradation processes [11-28]. SECM involves the use of a mobile ultramicroelectrode (UME) probe of micrometer dimension to investigate the activity and/or topography of an interface on a localized scale [29]. One of the modes of

SECM operation is the substrate generation/tip collection (SG/TC) mode, in which the substrate under study acts to generate species that are measured at the UME tip, which is held at a potential sufficient for a redox reaction to occur. SECM is an ideal tool for the investigation of local corrosion phenomena since it permits the possibility of precisely positioning the small UME tip close to the object under investigation, the active pit, in contrast to conventional methods frequently used to study pitting corrosion of passive metals, such as potentiodynamic polarization curves or electrochemical impedance spectroscopy (EIS).

The dissolution and pitting corrosion of iron and carbon steels [14, 22, 23, 27], as well as of stainless steels [11, 15, 17-20, 24, 28] have been investigated by SECM in several electrolytes containing $Cl^-$ anions. However, studies on pitting corrosion of stainless steels in the presence of $Br^-$ anions using SECM have not been found in the literature. Therefore, the aim of this study is to investigate the passive behavior and passivity breakdown of an austenitic stainless steel (AISI 304) in $Br^-$ containing solutions by means of SECM and Confocal Laser Scanning Microscopy.

## 2. EXPERIMENTAL PROCEDURE

### *2.1. Material and electrolyte*

The material tested was AISI 304 stainless steel (SS) (0.05 wt.% C, 18 wt.% Cr, 10 wt.% Ni, 0.4 wt.% Si, 0.1 wt.% N, Bal. Fe). AISI 304 SS electrodes were cylindrically shaped and covered with a polytetrafluoroethylene (PTFE) coating, to expose an area of 0.5 $cm^2$ to the test solution. All specimens were wet abraded from 200 to 4000 SiC grit,

and finally rinsed with distilled water and air-dried. AISI 304 SS electrodes were tested in two different naturally-aerated LiBr solutions: 0.2M and 0.6M, at a constant temperature of 25º C.

*2.2. Potentiodynamic polarization curves*

Cyclic potentiodynamic polarization curves of AISI 304 SS in the LiBr solutions were determined using a SOLARTRON 1287 potentiostat. The curves were repeated at least three times in order to verify reproducibility. The working electrode potential was measured vs. a silver-silver chloride (Ag/AgCl 3M KCl) reference electrode. The auxiliary electrode was a platinum wire. Before the tests, the specimen potential was reduced to -0.4 $V_{Ag/AgCl}$ in order to create reproducible initial conditions. Then, the electrode potential was scanned from -0.4 $V_{Ag/AgCl}$ in the positive direction at 0.5 mV $s^{-1}$. When the current density reached 10 mA $cm^{-2}$, the potential scan was reversed in order to evaluate the repassivation tendency.

From the *E*-log *i* plot, the corrosion potential ($E_{corr}$) and corrosion current density ($i_{corr}$) were obtained. The pitting potential ($E_p$) was evaluated using a criteria previously used in other studies [30], once the rapid and stable increase of the anodic current density occurs. The repassivation potential values ($E_{rp}$) were taken at the crossing between the backward scan and the forward scan [31]. Passive and repassivation current densities ($i_p$ and $i_{rp}$, respectively) were also obtained, being $i_p$ the current density in the passive domain and $i_{rp}$ the current density at $E_{rp}$.

*2.3. SECM measurements*

SECM tests were performed using a Sensolytics device connected to an Autolab AUT84192 bipotentiostat. A platinum ultramicroelectrode (UME) of 25 μm in diameter (the outer glass shield was 1.5 mm in diameter) was used as the SECM tip. Oxygen was used as the electrochemical mediator at the tip. The cyclic voltammogram was recorded at a scan rate of 50 mV $s^{-1}$ from 0 $V_{Ag/AgCl}$ to −1.2 $V_{Ag/AgCl}$. **Figure 1** shows the cyclic voltammogram of $O_2$ in the 0.2 M LiBr solution using the 25 μm platinum UME. A wide current plateau can be observed at potential values between -0.5 $V_{Ag/AgCl}$ and -1 $V_{Ag/AgCl}$, approximately, corresponding to the oxygen reduction reaction:

$$O_2 + 2H_2O + 4e^- \rightarrow 4OH^- \quad \textbf{(1)}$$

The curve displayed in **Figure 1** was used to choose the potential of the UME tip, which was set at -0.7 $V_{Ag/AgCl}$ to enable the diffusion-limited reduction of oxygen at the tip.

To study the influence of the applied potential on the passive behavior of AISI 304 SS, passive films were formed on its surface imposing different potentials within the passive range (0.0, 0.1 and 0.2 $V_{Ag/AgCl}$) for 1 hour.

The reduction of oxygen on the microelectrode was used to establish the height of the tip over the AISI 304 SS sample. After passive film formation, approach curves representing Current (I) vs. Distance between the UME tip and the surface of the sample (Z) were performed to select the best height of the UME tip. As an example, **Figure 2** shows an approach curve for the tip polarized at -0.7 $V_{Ag/AgCl}$ with the sample potential set at 0.0 V in the 0.2 M LiBr solution. The zero position of the tip, that is, the point

where the approach curves began, was an arbitrary position such that the influence of the specimen on the probe response was not significant. From this zero position the UME was moved down towards the sample and it stopped when the tip current reached 75% of the initial value in the bulk solution [25]. In order to prevent the tip from scratching the AISI 304 SS surface, due to roughness or small tilt of the sample, the distance between the UME and the substrate surface was afterwards increased by 5 μm. This increase in the tip-substrate distance by 5 μm resulted in an increase in the tip current by 8.33 %, in absolute value. Then, SECM scans were obtained by positioning the UME tip directly above and perpendicular to the sample and scanning the surface at steps of 250 μm in the X and Y directions. The scanned dimensions were 2000 μm × 2000 μm and the scan rate was 50 μm $s^{-1}$.

To study the initiation and formation of stable pits on the surface of the AISI 304 SS in the 0.2 M LiBr solution, the sample was subsequently biased at 0.45 $V_{Ag/AgCl}$, a potential close to the pitting potential. After the appearance of the first stable pit, different line scans were performed at different times by shifting the UME tip 3000 μm along the X direction passing just above the pit, at steps of 250 μm. Although the step size was significantly bigger than the tip diameter, this approach is acceptable in this case because the aim of the present work is not to resolve the surface to evidence precursor sites for pit nucleation, but to follow the propagation stages of a stable pit once nucleated. The tip potential remained set at -0.7 $V_{Ag/AgCl}$ to detect the electroactive species (metal cations) released from the localized corrosion site by reducing them at the UME tip, thus obtaining a cathodic current related to the activity within the pit. Using this mode of SECM operation, called sample generation – tip collection (SG-TC), the use of electrochemical mediators (i.e., an oxidizable/reducible species) that could

interact with the substrate, such as the redox couple $I^-/I_3^-$, is avoided, thus eliminating their interference with the corrosion reactions [11, 25, 29]. A 3D map of the surface around the pit was also obtained through scanning the surface at steps of 500 μm in the X and Y directions. The scanned dimensions were 3000 μm × 2000 μm in X and Y, respectively, with a scan rate of 50 μm $s^{-1}$.

After studying the formation and growth of a stable pit on the AISI 304 SS, the sample polarization was stopped to study pit repassivation at open circuit potential. Line scans and a 3D map of the surface were also obtained, following the same procedure explained above.

### *2.4. Confocal Laser Scanning Microscope measurements*

After potentiodynamic polarization curves, the AISI 304 SS samples were rinsed and examined with a Confocal Laser Scanning Microscope (CLSM) Olympus LEXT OLS3100, which uses the LEXT OLS 6.0.3 software. The CLSM uses a Laser Diode with a wavelength of 408 nm, an outstanding horizontal resolution of 0.22 μm, vertical resolution of 0.01 μm (z-axis), and a magnification range from 120x to 14400x.

The morphology of the pit formed on the AISI 304 SS electrode after the SECM measurements was also examined using the CLSM. The average pit radius and pit depth were quantified with the CLSM.

## 3. RESULTS AND DISCUSSION

177

178 *3.1. Potentiodynamic polarization curves*

179 **Table 1** shows the parameters determined from polarization curves (**Figure 3**) at two
180 different LiBr concentrations: 0.2M and 0.6M. As it can be seen in Table 1, an increase
181 in LiBr concentration from 0.2M to 0.6M slightly shifts corrosion potentials to more
182 active values and enhances corrosion current densities.

183 Polarization curves also provide information about the pitting, passivation and
184 repassivation behavior of the material. AISI 304 is susceptible to pitting corrosion since
185 bromides are very aggressive ions that promote SS passive film breakdown [30, 32, 33].
186 The lowest $E_p$ determined in the 0.6M LiBr solution indicates that bromides promote a
187 decrease in the pitting corrosion resistance and, consequently, the breakdown of the
188 passive film and the initiation of pits occur at less positive potentials.

189 **Table 1** shows that passive current densities are higher in the LiBr solution that
190 contains more bromides. **Table 1** also shows that repassivation current densities
191 obtained in both LiBr solutions are statistically the same. Since $i_{rp}$ is a measure of the
192 ability of materials to repassivate and, hence, of the extent of propagation once
193 corrosion has initiated, the previous results indicate that the ability of AISI 304 to
194 repassivate is essentially the same in both LiBr solutions. Additionally, $E_{rp}$ gives
195 information about the repassivation of the material after pitting; i.e., above $E_{rp}$ pits that
196 have initiated will continue to grow and at potentials below $E_{rp}$ pits repassivate. In the
197 present case, the corrosion potential is below $E_{rp}$, so pits can repassivate at potentials
198 between $E_{corr}$ and $E_{rp}$.

The surfaces of the stainless steel after the tests were examined with the CLSM. The number of pits together with their diameter is considerably greater in the test performed in the most concentrated solution, that is, $Br^-$ ions increase the pitting corrosion rate [34]. This result is in agreement with the parameters determined from polarization curves.

*3.2. Influence of passivation potential studied by SECM*

**Figure 4** shows the 3D maps of the AISI 304 SS surface biased at three different potentials among the passive range, i.e. 0, 0.1 and 0.2 $V_{Ag/AgCl}$ whereas the tip potential was set at -0.7 $V_{Ag/AgCl}$. **Figure 4(**a) and (b) represent the evolution of the current at the UME tip in the 0.2M and 0.6M LiBr solutions, respectively. The images correspond to 2000 μm × 2000 μm in *X* and *Y* directions. The plot in **Figure 4**(a) shows that current values determined at the UME tip are higher (in absolute value), compared to those obtained in the most concentrated LiBr solution (**Figure 4(**b)). This result seems to be reasonable since the solubility of oxygen diminishes with salinity (the experimental Henry's Law constants for oxygen in the 0.2M and 0.6M LiBr solutions at atmospheric pressure and 25º C are $4.54 \cdot 10^4$ atm. and $4.76 \cdot 10^4$ atm., respectively) [35]. Additionally, the current at the UME tip follows the same tendency with the applied potential in both concentrations; that is, it increases (in absolute value) as the potential is raised. The same tendency of the tip current obtained in both concentrations represents the reproducibility of the tests.

Passive films generally form as bilayers, with a highly disordered "barrier" layer adjacent to the metal and an outer film consisting of a precipitated phase that may incorporate anions and/or cations from the solution. Passivity is mainly attributed to the

barrier layer [36]. The passive films formed on stainless steels are considered highly doped semiconductors with dopant or defect densities [4, 37-39]. The protectiveness of the passive film is affected by the density of dopants or charge carriers and the latter is dependent on the applied potential in the passive domain. The passive film thus constitutes a barrier layer to ion transfer but not to electron transfer. Any redox electron transfer reaction is therefore allowed to occur on the passive film-covered metal surface just like on the metal surface without any film [40]. In fact, it is well known that the reduction of oxygen takes place in the formation of the passive film as cathodic reaction [41-43]. In this way, during the formation of the passive films, i.e. at the applied potentials shown in **Figure 4**, there should be a competition between the oxygen consumed in the corresponding cathodic reaction at the passive film on the stainless steel and at the UME tip. Taking into consideration that higher potentials promote an increase in the redox reaction rates [44, 45], a gradual decrease (in absolute value) in the tip current value with the applied potential, due to an increase of the oxygen reaction in the cathodic regions of the passive film, should be shown in **Figure 4**. However, **Figure 4** shows an opposite trend, that is, as the applied potential in the passive domain is increased, the current at the UME tip increases in absolute value. Therefore, the increase in absolute value of the tip current with the applied potential cannot be explained due to the presence of oxygen. Hence, other redox species that are influenced by the applied potential are interfering in the tip current. According to the Point Defect Model (PDM) [36, 46] the transmission of ions through the barrier layer occurs by vacancy motion, due to the preponderance of Schottky defects. Then, the following reactions may occur at the metal/film and film/solution interfaces [36, 47, 48]:

- Reactions at the metal/film interface:

$$m + V_M^{X'} \xrightarrow{k_1} M_M + v_m + Xe^- \quad (2)$$

$$m \xrightarrow{k_2} M_i^{X+} + v_m + Xe^- \quad (3)$$

$$m \xrightarrow{k_3} M_M + \frac{X}{2} V_O^{\bullet\bullet} + Xe^- \quad (4)$$

248

249 - Reactions at the film/solution interface:

$$M_M \xrightarrow{k_4} M^{\delta+} + V_M^{X'} + (\delta - X)e^- \quad (5)$$

$$M_i^{X+} \xrightarrow{k_5} M^{\delta+} + (\delta - X)e^- \quad (6)$$

$$V_O^{\bullet\bullet} + H_2O \xrightarrow{k_6} O_O + 2H^+ \quad (7)$$

$$MO_{X/2} + XH^+ \xrightarrow{k_7} M^{\delta+} + \frac{X}{2} H_2O + (\delta - X)e^- \quad (8)$$

250

251 where $m$ is a metal atom, $V_M^{X'}$ is a cation vacancy in the passive film, $M_i^{X+}$ is an
252 interstitial cation, $M_M$ is a metal cation in a cation site of the film, $v_M$ is a cation vacancy
253 in metal phase, $V_O^{\bullet\bullet}$ is an anion vacancy in the passive film, $O_O$ is an oxygen ion in the
254 passive film, $M^{+\delta}$ is a metallic cation in the electrolyte and $MO_{X/2}$ is the stoichiometric
255 passive film ($X$ is the oxidation state of the cations in the passive film and $\delta$ is the
256 oxidation state of the cations in the solution).

257

258 As the applied potential on the passive region of the stainless steel is increased, the rate
259 of the redox reactions is affected. Therefore, according to the reactions proposed in the
260 PDM, oxidation equations 2 to 6 and 8 could take place. However, in the system
261 proposed in this research, the charge of the cations in the oxides that form the passive

film ($X$) is equal to the charge of these cations in the solution (δ), hence only reactions shown in equations 2 to 4 occurring at the metal/film interface involve an exchange of electrons. The rate of the aforementioned redox reactions will increase as the applied potential is also increased [44, 45]. Thus, increasing the potential increases the rates of formation of metallic cations in the film ($M_M$, in equations 2 and 4) and of interstitial cations ($M_i^{X+}$ in equation 3). Furthermore, when the presence of these species in the passive film increases, the rate of the reactions taking place at the film/solution interface can be enhanced (equations 5 and 6), leading therefore to the formation of metallic cations in the solution ($M^{\delta+}$). As the number of metallic cations ejected from the metal to the solution increases, the current at the UME tip might also increase (in absolute value) and at its applied potential (-0.7 $V_{Ag/AgCl}$ = -0.495 $V_{NHE}$), the cations that reach the tip may be reduced.

The species that are present in the studied system are oxygen, water, bromide anions ($Br^-$) and lithium cations ($Li^+$) of the electrolyte and those cations coming from the passive film of the stainless steel. The $Br^-$ anions cannot be further reduced and the $Li^+$ cannot be reduced at the potential applied at the UME tip ($E^0_{Li+/Li}$ = -3.05 $V_{NHE}$). Moreover, neither water may be reduced to $H_2$ ($E^0_{H2O+/H2}$ = -0.83 $V_{NHE}$). Nevertheless, as it was previously mentioned, oxygen in neutral or alkaline media might be reduced to $OH^-$ ($E^0_{O2/OH-}$ = 0.40 $V_{NHE}$), but oxygen reduction cannot explain the results shown in **Figure 4**, as mentioned above. On the other hand, the main elements present in the AISI 304 (iron, chromium and nickel), may be in their different oxidation states depending on the applied potential among the passive region (0 to 0.2 $V_{Ag/AgCl}$ = 0.21-0.41$V_{NHE}$). Therefore, all the reactions with a standard electrode potential (reduction potential) lower than the applied passive potential might take place in the oxidation direction, that

is, the reduced form of the pair with lower potential will be oxidized. According to the standard electrode potentials, the iron, chromium and nickel species are stable at 0.21-0.41$V_{NHE}$ are $Fe^{+3}$ ($E^0_{Fe3+/Fe}$ = -0.036 $V_{NHE}$), $Fe^{+2}$ ($E^0_{Fe2+/Fe}$ = -0.44 $V_{NHE}$), $Ni^{+2}$ ($E^0_{Ni2+/Ni}$ = -0.23 $V_{NHE}$) and $Cr^{+3}$ ($E^0_{Cr3+/Cr}$ = -0.73 $V_{NHE}$). Thus, from a thermodynamic point of view the cations ejected from the passive film formed on the stainless steel in our study may be $Fe^{+2}$, $Fe^{+3}$, $Ni^{+2}$ and $Cr^{+3}$. Then, in order to relate the current at UME tip with the reduction of some species, it is necessary to know which of the aforementioned cations would be reduced at -0.7 $V_{Ag/AgCl}$ = -0.495 $V_{NHE}$, i.e. the potential held at the UME tip. Any reduction reaction with a standard electrode potential higher than -0.495 $V_{NHE}$ might take place in our system. The following reactions may occur:

$$Fe^{2+} + 2e^- \rightarrow Fe \ (E^0_{Fe2+/Fe} = -0.44\ V_{NHE}) \quad (9)$$

$$Ni^{2+} + 2e^- \rightarrow Ni \ (E^0_{Ni2+/Ni} = -0.23\ V_{NHE}) \quad (10)$$

$$Fe^{3+} + 3e^- \rightarrow Fe \ (E^0_{Fe3+/Fe} = -0.036\ V_{NHE}) \quad (11)$$

$$Fe^{3+} + e^- \rightarrow Fe^{2+} \ (E^0_{Fe3+/Fe2+} = 0.77\ V_{NHE}) \quad (12)$$

Note that in order to reduce $Cr^{3+}$ to metallic Cr, more negative potentials are needed (-0.73 $V_{NHE}$).

According to the literature [7, 8, 49] nickel has not been found in the composition of AISI 304 or AISI 316 SS passive films. Hence, the possible reactions at the UME tip (apart from the reduction of $O_2$ to $OH^-$, which is always present in our system, see **Figure 1**) are those involving iron species ($Fe^{+2}$ and $Fe^{+3}$). In this way, a logical explanation of the tendency observed in **Figure 4** (i.e., the current of the UME tip increases in absolute value as the potential also increases), might be the higher amount of iron cations ejected from the passive film and available at the UME tip due to an

increase in the applied potential. Then, at higher potentials more cations are reduced to iron (equations 8 and 10) at the UME tip which is held at -0.7 $V_{Ag/AgCl}$ [14].

*3.3. SECM imaging of active pitting corrosion and repassivation*

To study the initiation and formation of stable pits on the surface of the AISI 304 SS in 0.2 M LiBr solution, different potentials were selected and applied to the substrate (in the passive region but close to the value of $E_p$ determined from polarization curves in **Figure 3**). The lowest potential at which a stable pit appeared was 0.45 $V_{Ag/AgCl}$, so the sample was biased at this value. After the appearance of the first stable pit, different line scans of 3000 μm each were performed just above the pit, setting the UME tip potential at -0.7 $V_{Ag/AgCl}$. To perform these experiments, a test solution of 0.2 M LiBr has been chosen instead of 0.6 M LiBr to minimize the appearance of pits on the electrode surface when imposing a potential close to $E_p$.

**Figure 5** shows the line scans at different polarization times. It can be observed that, regardless of the polarization time, the currents recorded when the tip passed just over the center of the pit (X = 1500 μm) were significantly higher (in absolute value) than the currents measured over the areas covered with an undamaged passive film. Souto et al [25, 26], working with polymer-coated carbon steel plates, also observed an increase in the current measured at the tip when it passed over a circular defect artificially produced in the organic coating. They explained these results in terms of an enhancement of the amount of soluble oxygen available from the electrolyte volume inside the hole, since the substrate surface was no longer obstructing the diffusion of

oxygen from the bulk. Consequently, the currents measured at the UME tip over the defect were of the same order of magnitude as that recorded in the bulk solution for oxygen reduction. In the present case, however, currents recorded at the tip near the active pit were far more negative than those observed in the bulk solution associated with the reduction of oxygen at the UME tip (which are of the order of -2 nA, see **Figure 2**).

On the other hand, since a process of active corrosion was taking place inside the pit (the current of the substrate increased drastically just before the appearance of the stable pit), a redox competition for dissolved oxygen could be expected to occur inside the pit between the UME tip and the bare steel surface. According to Souto et al [21, 25, 26], the concentration of oxygen available to be reduced at the tip will decrease near a corroding surface, such as inside an active pit, due to the appearance of cathodic sites where oxygen can be consumed. Assuming that it is the $O_2$ reduction reaction that is taking place at the tip, a decrease in the amount of oxygen available at the tip would lead to a decrease (in absolute value) in the tip current. However, such a decrease in the tip current near the active pit with respect to the background current is not observed in **Figure 5**.

Inside a stable pit the characteristics of the electrolyte are different from those in bulk solution [31]. The local environment becomes enriched in metal cations and anionic species such as bromides or chlorides, and the pH is lower owing to cation hydrolysis. This fact makes pitting autocatalytic, that is, once a pit becomes stable, it grows at an ever-increasing rate without any external stimulus [2, 31]. During active corrosion of iron and stainless steels (such as AISI 304 SS), $Fe^{2+}$ cations are produced inside the pits

[11, 14, 24, 50]. Other cations such as $Cr^{3+}$ and $Ni^{2+}$ can also be produced inside active pits formed on stainless steels [28, 51]. The high currents measured at the UME tip when it was located just over the pit suggest an active corrosion process inside the pit releasing metal cations and a subsequent reduction of those cations at the UME tip [11, 14], which was biased at -0.7 $V_{Ag/AgCl}$. Protons may also be simultaneously reduced at the tip [14, 52].

To confirm the explanations given above concerning the reduction process taking place at the tip, **Figure 6** shows a cyclic voltammogram taken while the tip was positioned near the active corrosion pit. Comparing the voltammogram after corrosion with that recorded in the solution bulk before corrosion (initial in **Figure 6**), it can be clearly observed that cathodic currents greatly increased after the corrosion process. This result indicates the presence of high amounts of other reducible species (metal cations) apart from oxygen.

It can be observed from **Figure 5(a)** that at short polarization times the tip current reached very negative and approximately constant values, but it started decreasing after 70 seconds. This behavior can be explained taking into account the precipitation of a salt film on the pit surface [31, 51, 53, 54]. The high cathodic currents recorded at short polarization times imply a very high metal dissolution rate (in fact, higher than the diffusion rate of cations from the pit towards the UME tip) leading to an increase in the ionic concentration inside the pit and to eventually reaching supersaturation conditions [31, 51]. This salt layer decreased metal dissolution since it acted as a diffusion barrier and hence the process of pit growth became limited by mass transport.

However, at longer polarization times (from 210 seconds on), the tip current began to increase again (**Figure 5(b)**) although it never reached values as high as those measured at the beginning of the test, when metal dissolution was very intense. **Figure 7** compares the values of the tip current measured just over the active pit at $X$ = 1500 μm at different polarization times. It can be observed that $I_{pit}$ values were very high in the beginning (in absolute value), indicating a very fast dissolution inside the active pit which led to an increase in the concentration of metal cations inside the pit (A in **Figure 7**) [31, 51]. Eventually, supersaturation conditions were reached and a solid salt layer formed on the pit surface, leading to a considerable decrease in the tip current over the pit (B in **Figure 7**) [31, 51]. After the sudden drop in $I_{pit}$ due to the precipitation of the salt film on the pit surface, the current value increased again following a linear tendency with time (C in **Figure 7**). This displacement of current towards higher values (in absolute value) with increasing polarization time is consistent with an active process of corrosion taking place inside the pit and is directly related to pit propagation [23]. Moreover, the previous results imply that after 210 seconds of active pitting corrosion, the salt layer formed on the pit surface no longer acted as a diffusion barrier, since a continuous increase in the release of metallic cations from the active pit and their subsequent reduction at the UME tip was observed.

It is worth mentioning that an increase in the background current with increasing polarization times can be observed in **Figure 5**, which is associated with the accumulation and slow diffusion of metallic cations released from the substrate towards the bulk solution [24, 55]. Hence, at long polarization times, small amounts of these cations can be reduced at the UME tip far from the pit. However, the ratio between the current over the active pit and the background current is very high and it increases with

immersion time, which indicates that changes in the background current with time are very small compared to the changes of the tip current measured above the active pit.

Once the growth of the active pit with time has been studied, the next step is to study the repassivation of the pit when stopping potentiostatic polarization. As in the previous case, different line scans were carried out above the repassivating pit, with the tip potential set at -0.7 $V_{Ag/AgCl}$ and leaving the AISI 304 SS substrate at open circuit potential. **Figure 8** shows the line scans at different repassivation time.

It can be observed from **Figure 8(a)** that immediately after stopping polarization the cathodic current measured at the UME tip sharply decreased (in absolute value). After that (**Figure 8**) the tip current measured above the pit became less negative with repassivation time until it reached approximately constant values along the scan length after 160 seconds. These results reveal a total repassivation of the existing pit, since its propagation ceased completely. Final values of the tip current are slightly higher than those recorded before the onset of pitting corrosion on the substrate at 0.45 $V_{Ag/AgCl}$. As it has been mentioned above, this difference in background current with time is explained by the gradual accumulation of metallic cations released from the metal substrate.

The previous results show that the pit formed on AISI 304 SS under potentiostatic polarization was no longer stable at open circuit potential and stopped propagating. Pit stability depends, among other things, on the maintenance of pit electrolyte composition and pit bottom potential [31, 56]. If a salt film is formed on the pit bottom, the pit growth rate will be diffusion controlled. Under these circumstances, a decrease in the potential may not lead to repassivation and pits may continue to grow, depending on the

composition of the pit electrolyte [31, 56]. The formation of a salt film has been cited above as a likely reason to explain the decrease in the tip current with polarization time after reaching very negative values (**Figure 5(a)** and **Figure 7**). However, at longer polarization times (from 210 seconds on) the salt layer no longer influenced pit growth, since the current associated with the cations released from the pit bottom started to increase again (in absolute value) (**Figure 7**). Therefore, the complete repassivation of the dissolving metal surface at the pit bottom after 160 seconds at open circuit potential indicates that, in the system under study and after some time of potentiostatic pit growth, charge-transfer processes inside the pit played an essential role in its stability.

**Figure 9** shows the 3D maps of the AISI 304 SS surface obtained at the end of the pit activation process at 0.45 $V_{Ag/AgCl}$ (**Figure 9(a)**) and at the end of the pit repassivation process at open circuit potential (**Figure 9(b)**). The images represent 3000 μm × 2000 μm in *X* and *Y* directions, respectively. The plot in **Figure 9(a)** clearly shows the generation and release of metal cations from a single pit centered in the point (X = 1500 μm; Y = 1000 μm) and reduced afterwards at the UME tip, whose potential was set at -0.7 $V_{Ag/AgCl}$. It can be observed from **Figure 9(b)** that the formation of $Fe^{2+}$ and other cationic species from the pit was effectively stopped at open circuit potential, since at the point (X = 1500 μm; Y = 1000 μm) the tip current was similar to the background current, indicating a complete repassivation of the pit.

**Figure 10** shows the 2D image of the pit formed on the AISI 304 SS surface in 0.2 M LiBr solution at 0.45 $V_{Ag/AgCl}$, obtained with a CLSM. In order to visualize the pit morphology and to quantify its depth, two profiles (longitudinal and transversal) were also obtained. It can be observed from the 2D image (**Figure 10(a)**) that the pit mouth

had an approximately equiaxed (circular) shape, bounded by facets. According to Newman and Franz, it is possible that this pit grew initially by coalescence from several nucleation points [51]. The average radius of the pit was estimated to be 99.8 ± 0.7 μm. It can also be observed from both profiles (**Figures 10(b)** and **10(c)**) that the bottom of the pit was not uniform. The average pit depth was 8.0 ± 0.9 μm.

It is evident from the above calculations that the pit radius was far higher than the pit depth, indicating that this pit was not hemispherical but dish-shaped. Some authors working with stainless steels have observed a change in the pit shape from hemispherical to dish-shaped during their growth [57-61]. According to Newman [58, 60, 61], early pit growth takes place in a hemispherical mode under the remnants of an overhanging passive film; when a pit reaches a critical size, this cover is destroyed and the hemispherical cavity is opened to the bulk solution. Hence, large pits (of the order of several tens or even hundreds of μm in diameter) have been usually found to be dish-shaped rather than perfectly hemispherical, because the absence of a pit cover makes the hemispherical shape unstable, resulting in a faster dissolution rate at the pit edges [31, 58, 60-63]. These explanations are consistent with the SECM and CLSM observations of the pit formed on AISI 304 SS, which presented a dish-shaped morphology.

## CONCLUSIONS

An increase in LiBr concentration from 0.2M to 0.6M enhances the passive current density and lowers the pitting potential.

As the applied potential in the passive domain is increased, the current at the UME tip increases in absolute value. This increase can be explained due to the enhancement of metallic cations at the film/solution interface at high potentials, according to the Point Defect Model. As the number of metallic cations ejected from the metal to the solution increases, the current at the UME tip might also increase.

The tip currents recorded over the center of the pit were significantly higher (in absolute value) than the currents measured over the areas covered with an undamaged passive film. This fact can be explained by an active corrosion process taking place inside the pit, resulting in the release of metal cations and their subsequent reduction at the UME tip.

The evolution of the tip current over the active pit with polarization time suggested a very high metal dissolution rate during the first 70 seconds and then the precipitation of a salt film on the pit surface after reaching supersaturation conditions. At longer polarization times the tip current began to increase again indicating that an active corrosion process was occurring inside the pit.

Immediately after stopping polarization the cathodic current measured at the UME tip sharply decreased (in absolute value) and became less negative with repassivation time until it reached approximately constant values. These results reveal a total repassivation of the existing pit.

The pit radius was observed to be far higher than the pit depth, indicating that this pit was not hemispherical but dish-shaped. This morphology is consistent with the loss of

the pit cover (a salt layer or the remnants of an overhanging passive film) and the preferential dissolution at the pit edges, leading to a change in pit shape from perfectly hemispherical at the first stages of pit growth to a dish-shaped form at longer times.

## ACKNOWLEDGEMENTS

The authors would like to express their gratitude to the Generalitat Valenciana for its help in the SECM acquisition (PPC/2011/013) and in the CLSM acquisition (MY08/ISIRM/S/100) and to Dr. Asuncion Jaime for her translation assistance.

## REFERENCES

[1] Harold M.Cobb (Ed.), Steel Products Manual: Stainless Steels, Iron & Steel Society, 1999.

[2] P. A. Schweitzer, Corrosion Engineering Handbook: Fundamentals of Metallic Corrosion, CRC Press, Boca Ratón, FL., 2007.

[3] A. J. Sedriks, Corrosion Resistance of Stainless Steels and Nickel Alloys, in: S.D. Cramer, B.S. Covino, Jr. (Eds.), Corrosion: Fundamentals, Testing and Protection, Vol. 13A, ASM Handbook, ASM International, Materials Park, OH, 2003, p. 697-702.

[4] N. E. Hakiki, S. Boudin, B. Rondot, M. Da Cunha Belo. The electronic structure of passive films formed on stainless steels, Corros. Sci. 37 (1995) 1809-1822.

[5] T. L. S. Wijesinghe, D. J. Blackwood. Photocurrent and capacitance investigations into the nature of the passive films on austenitic stainless steels, Corros. Sci. 50 (2008) 23-34.

[6] N. E. Hakiki, M. Da Cunha Belo, A. M. P. Simões, M. G. S. Ferreira. Semiconducting Properties of Passive Films Formed on Stainless Steels, J. Electrochem. Soc. 145 (1998) 3821-3829.

[7] I. Olefjord, B. Brox, U. Jelvestam. Surface Composition of Stainless Steels during Anodic Dissolution and Passivation Studied by ESCA, J. Electrochem. Soc. 132 (1985) 2854-2861.

[8] G. Lothongkum, S. Chaikittisilp, A. W. Lothongkum. XPS investigation of surface films on high Cr-Ni ferritic and austenitic stainless steels, Appl. Surf. Sci. 218 (2003) 203-210.

[9] L. Freire, M. J. Carmezim, M. G. S. Ferreira, M. F. Montemor. The passive behavior of AISI 316 in alkaline media and the effect of pH: A combined electrochemical and analytical study, Electrochim. Acta 55 (2010) 6174-6181.

[10] P. R. Roberge, Corrosion Engineering. Principles and Practice, 1st. ed., McGraw-Hill, New York, NY, 2008.

[11] D. O. Wipf, Initiation and study of localized corrosion by scanning electrochemical microscopy, Colloid Surface A 93 (1994) 251-261.

[12] N. Casillas, S. Charlebois, W. H. Smyrl, H. S. White, Pitting Corrosion of Titanium, J. Electrochem. Soc. 141 (1994) 636-642.

[13] S. B. Basame, H. S. White, Scanning Electrochemical Microscopy of Native Titanium Oxide Films. Mapping the Potential Distribution of Spatially-Localized Electrochemical Reactions, J. Phys. Chem. 99 (1995) 16430-16435.

[14] J. W. Still, D. O. Wipf, Breakdown of the Iron Passive Layer by Use of the Scanning Electrochemical Microscope, J. Electrochem. Soc. 144 (1997) 2657-2665.

[15] Y. Zhu, D. E. Williams, Scanning Electrochemical Microscopic Observation of a Precursor State to Pitting Corrosion of Stainless Steel, J. Electrochem. Soc. 144 (1997) L43-L45.

[16] S. B. Basame, H. S. White, Scanning electrochemical microscopy: measurement of the current density at microscopic redox-active sites on titanium, J. Phys. Chem. B 102 (1998) 9812-9819.

[17] D. E. Williams, T. F. Mohiuddin, Y. Y. Zhu, Elucidation of a Trigger Mechanism for Pitting Corrosion of Stainless Steels Using Submicron Resolution Scanning Electrochemical and Photoelectrochemical Microscopy, J. Electrochem. Soc. 145 (1998) 2664-2672.

[18] T. E. Lister, P. J. Pinhero, Scanning Electrochemical Microscopy Study of Corrosion Dynamics on Type 304 Stainless Steel, Electrochem. Solid St. 5 (2002) B33-B36.

[19] T. E. Lister, P. J. Pinhero, The effect of localized electric fields on the detection of dissolved sulfur species from Type 304 stainless steel using scanning electrochemical microscopy, Electrochim. Acta 48 (2003) 2371-2378.

572 [20] Y. González-García, G. T. Burstein, S. González, R. M. Souto, Imaging
573 metastable pits on austenitic stainless steel in situ at the open-circuit corrosion
574 potential , Electrochem. Commun. 6 (2004) 637–642.

575 [21] R. M. Souto, Y. González-García, S. González, In situ monitoring of
576 electroactive species by using the scanning electrochemical microscope.
577 Application to the investigation of degradation processes at defective coated
578 metals, Corros. Sci. 47 (2005) 3312-3323.

579 [22] E. Völker, C. González Inchauspe, E. J. Calvo, Scanning electrochemical
580 microscopy measurement of ferrous ion fluxes during localized corrosion of
581 steel, Electrochem. Commun. 8 (2006) 179–183.

582 [23] C. Gabrielli, S. Joiret, M. Keddam, H. Perrot, N. Portail, P. Rousseau, V.
583 Vivier, A SECM assisted EQCM study of iron pitting, Electrochim. Acta 52
584 (2007) 7706-7714.

585 [24] Y. Yin, L. Niu, M. Lu, W. Guo, S. Chen, In situ characterization of localized
586 corrosion of stainless steel by scanning electrochemical microscope, Appl.
587 Surf. Sci. 255 (2009) 9193-9199.

588 [25] J. J. Santana, J. González-Guzmán, L. Fernández-Mérida, S. González, R. M.
589 Souto, Visualization of local degradation processes in coated metals by means
590 of scanning electrochemical microscopy in the redox competition mode,
591 Electrochim. Acta 55 (2010) 4488-4494.

592 [26] Y. González-García, J. J. Santana, J. González-Guzmán, J. Izquierdo, S.
593 González, R. M. Souto, Scanning electrochemical microscopy for the

investigation of localized degradation processes in coated metals, Prog. Org. Coat. 69 (2010) 110-117.

[27] Y. Yuan, L. Li, C. Wang, Y. Zhu, Study of the effects of hydrogen on the pitting processes of X70 carbon steel with SECM, Electrochem. Commun. 12 (2010) 1804-1807.

[28] N. Aouina, F. Balbaud-Célérier, F. Huet, S. Joiret, H. Perrot, F. Rouillard, V. Vivier, Single pit initiation on 316L austenitic stainless steel using scanning electrochemical microscopy, Electrochim. Acta 56 (2011) 8589-8596.

[29] A. J. Bard, M. V. Mirkin (Eds.), Scanning Electrochemical Microscopy, 1st. ed., Marcel Dekker, New York, NJ, 2001.

[30] M. Kaneko, H.S. Isaacs, Pitting of stainless steel in bromide, chloride and bromide/chloride solutions, Corros. Sci 42 (2000) 67-78.

[31] G. S. Frankel, Pitting Corrosion of Metals: A Review of the Critical Factors, J. Electrochem. Soc. 145 (1998) 2186-2198.

[32] M. Kaneko, H.S. Isaacs, Effects of molybdenum on the pitting of ferritic- and austenitic-stainless steels in bromide and chloride solutions, Corros. Sci. 44 (2002) 1825-1834.

[33] E. A. Abd EI Meguid, N. A. Mahmoud, Inhibition of Bromide-Pitting Corrosion of Type 904L Stainless Steel, Corrosion 59 (2003) 104-111.

[34] A. Anderko and R. D. Young, Model for Corrosion of Carbon Steel in Lithium Bromide Absorption Refrigeration Systems, Corrosion 56 (2000) 543-555.

[35] D. S. Chau, B. D. Wood, N. S. Berman, K. J. Kim, Solubility of oxygen in aqueous lithium bromide using electrochemical technique, Int. Comm. Heat Mass Transfer 20 (1993) 643-652.

[36] D. D. Macdonald, The Point Defect Model for the Passive State, J. Electrochem. Soc.139 (1992) 3434-3449.

[37] A. Di Paola, Semiconducting properties of passive films on stainless steels, Electrochim. Acta 34 (1989) 203-210.

[38] N.E. Hakiki, M.F. Montemor, M.G.S. Ferreira, M. da Cunha Belo, Semiconducting properties of thermally grown oxide films on AISI 304 stainless steel, Corros Sci 42 (2000) 687-702.

[39] M.J. Carmezim, A.M. Simões, M.O. Figueiredo, M. Da Cunha Belo, Electrochemical behavior of thermally treated Cr-oxide films deposited on stainless steel, Corros Sci 44 (2002) 451-465.

[40] S. K. Sharma, Green Corrosion Chemistry and Engineering: Opportunities and Challenges, Wiley-VCH Verlag GmbH & Co., First Edition, Germany, 2012.

[41] M. S. Venkatraman, I. S. Cole, B. Emmanuel, Corrosion under a porous layer: A porous electrode model and its implications for self-repair, Electrochim Acta 56 (2011) 8192-8203.

[42] S. Thomas, I.S. Cole, M. Sridhar, N. Birbilis, Revisiting zinc passivation in alkaline solutions, Electrochim Acta 97 (2013) 192-201.

[43] S. Gao, C. Dong, H. Luo, K. Xiao, X. Pan, X. Li, Scanning electrochemical microscopy study on the electrochemical behavior of CrN film formed on 304 stainless steel by magnetron sputtering, Electrochim Acta 114 (2013) 233-241.

[44] G. Lu, J. S. Cooper, P. J. McGinn, SECM imaging of electrocatalytic activity for oxygen reduction reaction on thin film materials, Electrochimica Acta 52 (2007) 5172–5181.

[45] C. Song, J. Zhang, Electrocatalytic Oxygen Reduction Reaction, in: J. Zhang (Ed.), PEM Fuel Cell Electrocatalysts and Catalyst Layers, Ch. 2, Springer, London, 2008, p. 89.

[46] D. D. Macdonald, Passivity - the key to our metals-based civilization, Pure Appl. Chem. 71 (1999) 951-978.

[47] D. D. Macdonald, M. Al Rifaie, G. R. Engelhardt, New Rate Laws for the Growth and Reduction of Passive Films, J. Electrochem. Soc. 148 (2001) B343-B347.

[48] D. D. Macdonald, On the Existence of Our Metals-Based Civilization: I. Phase-Space Analysis, J. Electrochem. Soc. 153 (2006) B213-B224.

[49] C. Marconnet, Y. Wouters, F. Miserque, C. Dagbert, J. P. Petit, A. Galerie, Chemical composition and electronic structure of the passive layer formed on stainless steels in a glucose-oxidase solution D. Féron, Electrochim. Acta 54 (2008) 123-132.

655 [50] S. Rhode, V. Kain, V.S. Raja, G.J. Abraham, Factors affecting corrosion
656 behavior of inclusion containing stainless steels: A scanning electrochemical
657 microscopic study, Materials Characterization 77 (2013) 109-115

658 [51] R.C. Newman, E.M. Franz, Growth and repassivation of single corrosion pits
659 in stainless steel, Corrosion 40 (1984) 325-330.

660 [52] A.M. Simões, A.C. Bastos, M.G. Ferreira, Y. González-García, S. González,
661 R.M. Souto, Use of SVET and SECM to study the galvanic corrosion of an
662 iron–zinc cell, Corros. Sci. 49 (2007) 726-739.

663 [53] T. R. Beck, R. C. Alkire, Occurrence of Salt Films during Initiation and
664 Growth of Corrosion Pits, J. Electrochem. Soc. 126 (1979) 1662-1666.

665 [54] Richard C. Alkire, Kai P. Wong, The corrosion of single pits on stainless steel
666 in acidic chloride solution, Corros. Sci. 28 (1988) 411-421.

667 [55] A.C. Bastos, A.M. Simões, S. González, Y. González-García, R.M. Souto,
668 Imaging concentration profiles of redox-active species in open-circuit
669 corrosion processes with the scanning electrochemical microscope,
670 Electrochem. Commun. 6 (2004) 1212-1215.

671 [56] H. Böhni, Localized Corrosion of Passive Metals, in: R. Winston Revie (Ed.),
672 Uhlig's Corrosion Handbook, 2nd ed., Ch. 10, Wiley Interscience, New York,
673 2000.

674 [57] R. Leiva-García, J. García-Antón, M.J. Muñoz-Portero Contribution to the
675 elucidation of corrosion initiation through confocal laser scanning microscopy
676 (CLSM), Corros. Sci. 52 (2010) 2133-2142.

[58] N.J. Laycock, R.C. Newman, Localized dissolution kinetics, salt films and pitting potentials, Corros. Sci. 39 (1997) 1771-1790.

[59] M. H. Moayed, R. C. Newman, The Relationship Between Pit Chemistry and Pit Geometry Near the Critical Pitting Temperature, J. Electrochem. Soc. 153 (2006) B330-B335.

[60] P. Ernst, R.C. Newman, Pit growth studies in stainless steel foils. I. Introduction and pit growth kinetics, Corros. Sci. 44 (2002) 927-941.

[61] P. Ernst, N.J. Laycock, M.H. Moayed, R.C. Newman, The mechanism of lacy cover formation in pitting, Corros. Sci. 39 (1997) 1133-1136.

[62] D. Sun, Y. Jiang, Y. Tang, Q. Xiang, C. Zhong, J. Liao, J. Li, Pitting corrosion behavior of stainless steel in ultrasonic cell, Electrochim. Acta 54 (2009) 1558-1563.

[63] J. Ren, Y. Zuo, The growth mechanism of pits in NaCl solution under anodic films on aluminum, Surf. Coat. Tech. 191 (2005) 311-316.

Table captions

**Table 1**. Electrochemical parameters for AISI 304 SS in both 0.2 and 0.6 M LiBr solutions, obtained from cyclic polarization curves

Figures captions

**Figure 1**. Cyclic voltammogram measured at the SECM tip of the AISI 304 SS in the 0.2 M LiBr solution at 25 °C.

**Figure 2**. Approach curve for the tip polarized at -0.7 $V_{Ag/AgCl}$ with the AISI 304 SS potential set at 0 V in the 0.2 M LiBr solution.

**Figure 3**. Cyclic potentiodynamic polarization curves for AISI 304 in both 0.2 and 0.6 M LiBr solutions at 25º C.

**Figure 4**. SECM-3D maps of the AISI 304 SS surface biased at 0, 0.1 and 0.2 $V_{Ag/AgCl}$ in the 0.2M (a) and 0.6M (b) LiBr solutions.

**Figure 5**. Line scans on a pit formed on the AISI 304 biased at 0.45 $V_{Ag/AgCl}$ in a 0.2 M LiBr solution.

**Figure 6**. Cyclic voltammogram measured near an active corrosion pit and initially at the SECM tip of the AISI 304 SS in the 0.2 M LiBr solution.

**Figure 7**. Current values at the tip current measured on an active pit at different polarization times.

**Figure 8**. Line scans on the AISI 304 maintained at open circuit potential at different repassivation times in the 0.2 M LiBr solution.

**Figure 9**. SECM-3D maps of the AISI 304 SS surface at the end of the pit activation process at 0.45 $V_{Ag/AgCl}$ (a) and at the end of the pit repassivation process at open circuit potential (b).

718 **Figure 10**. CLSM-2D image of a pit formed on the AISI 304 SS surface in the 0.2 M
719 LiBr solution at 0.45 $V_{Ag/AgCl}$ (a). X and Y depth profiles are shown in (b) and (c),
720 respectively.

721

722

723

724

| LiBr Solution | $E_{corr}$/mV vs (Ag/AgCl) | $i_{corr}$/μA $cm^{-2}$ | $i_p$/μA $cm^{-2}$ | $E_p$/mV vs (Ag/AgCl) | $E_{rp}$/mV vs (Ag/AgCl) | $i_{rp}$/μA $cm^{-2}$ |
|---|---|---|---|---|---|---|
| **0.2 M** | -124 ± 7 | 0.3 ± 0.1 | 2.3 ± 0.2 | 557 ± 10 | 164 ± 10 | 5.3 ± 0.1 |
| **0.6 M** | -147 ± 10 | 0.6 ± 0.1 | 3.1 ± 0.2 | 496 ± 8 | 145 ± 12 | 6.3 ± 0.2 |

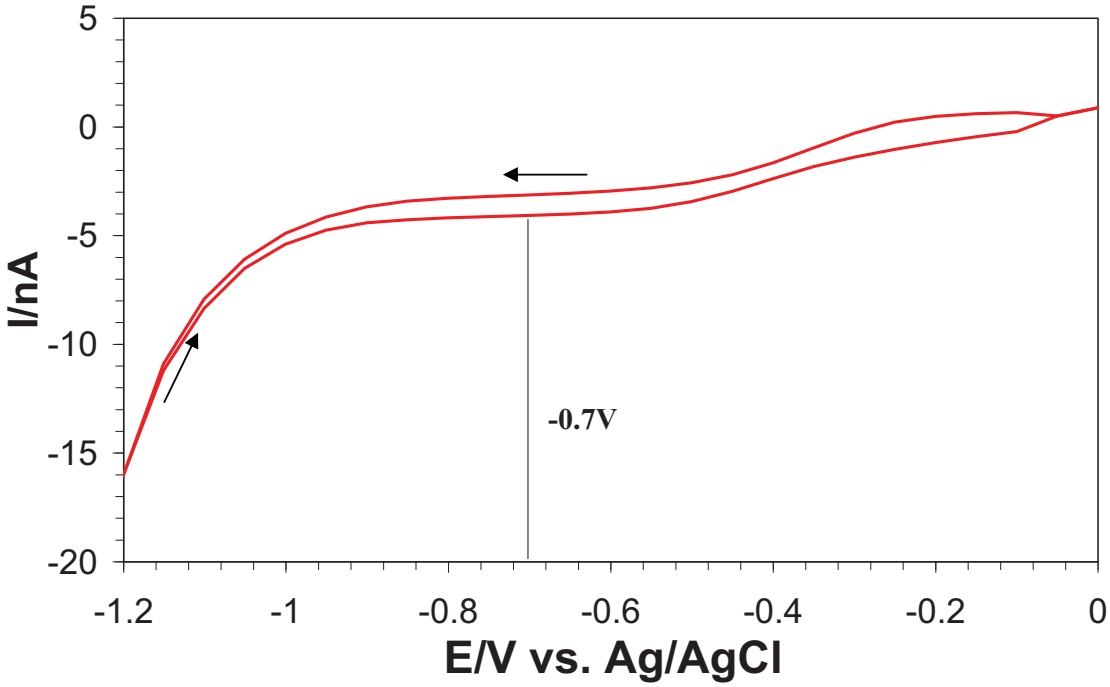
5
0
-5
-10
-15
-20
I/nA
-1.2
-1
-0.8
-0.6
-0.4
-0.2
0
E/V vs. Ag/AgCl
-0.7V

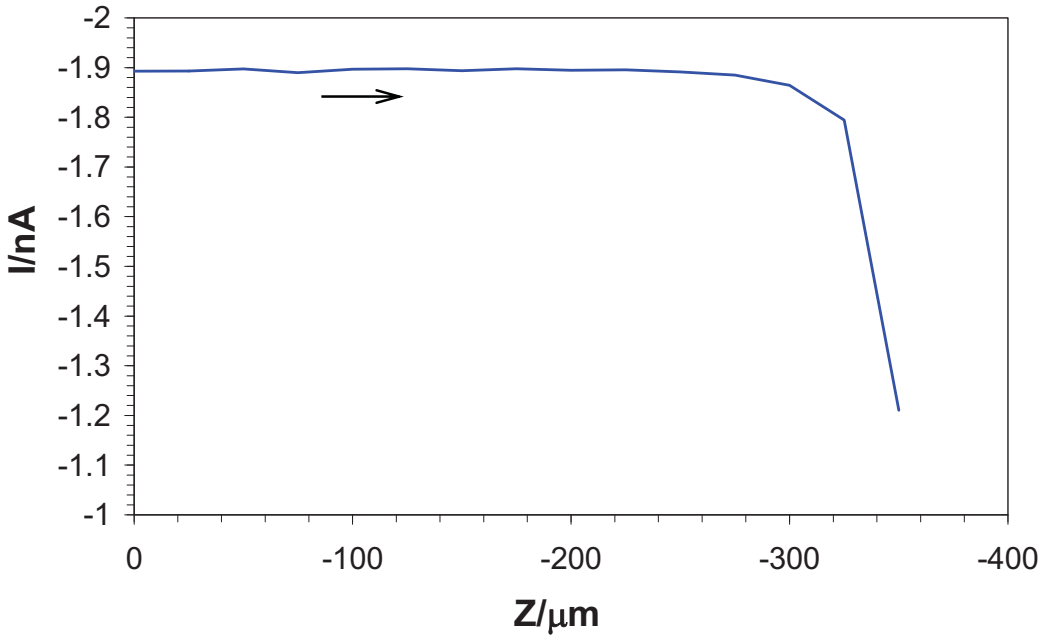
-2
-1.9
-1.8
-1.7
-1.6
-1.5
-1.4
-1.3
-1.2
-1.1
-1
I/nA
0
-100
-200
-300
-400
Z/μm

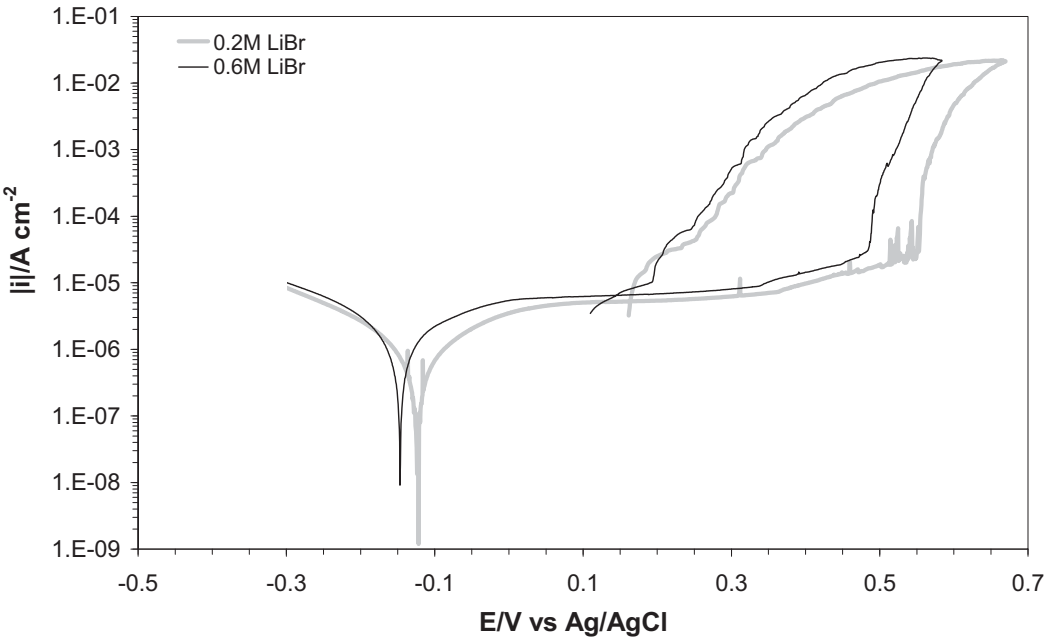
0.2M LiBr
0.6M LiBr
1.E-01
1.E-02
1.E-03
1.E-04
1.E-05
1.E-06
1.E-07
1.E-08
1.E-09
|i|/A cm-2
-0.5
-0.3
-0.1
0.1
0.3
0.5
0.7
E/V vs Ag/AgCl

(a) 0.2M LiBr

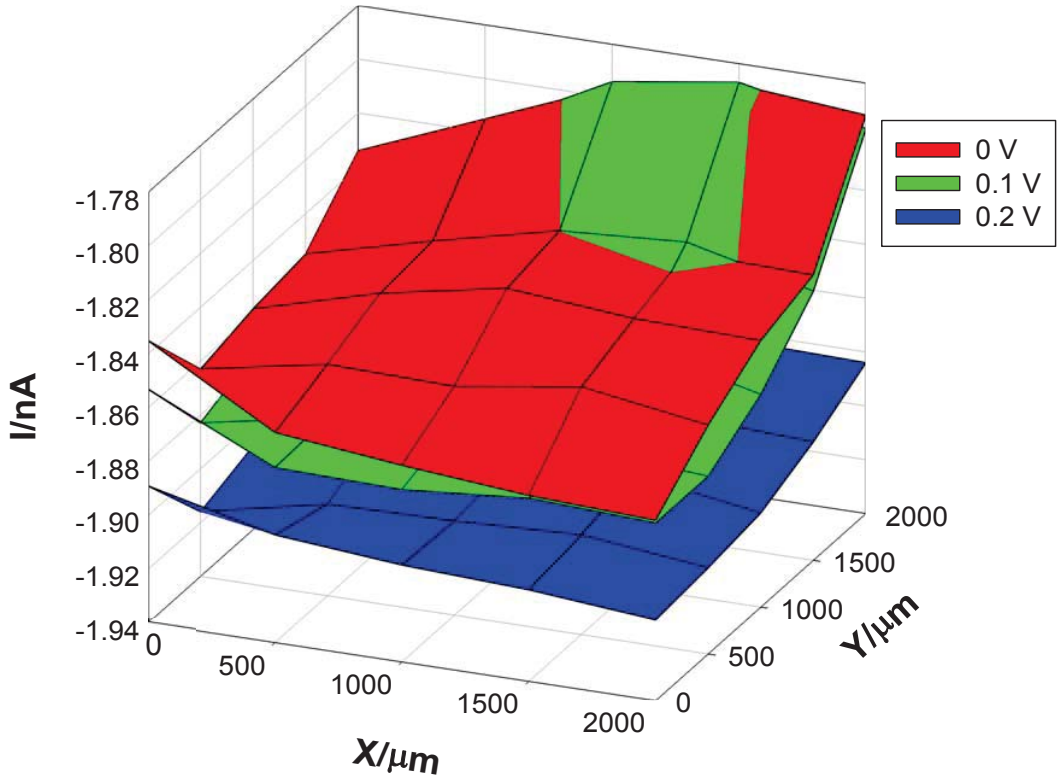


(b) 0.6M LiBr

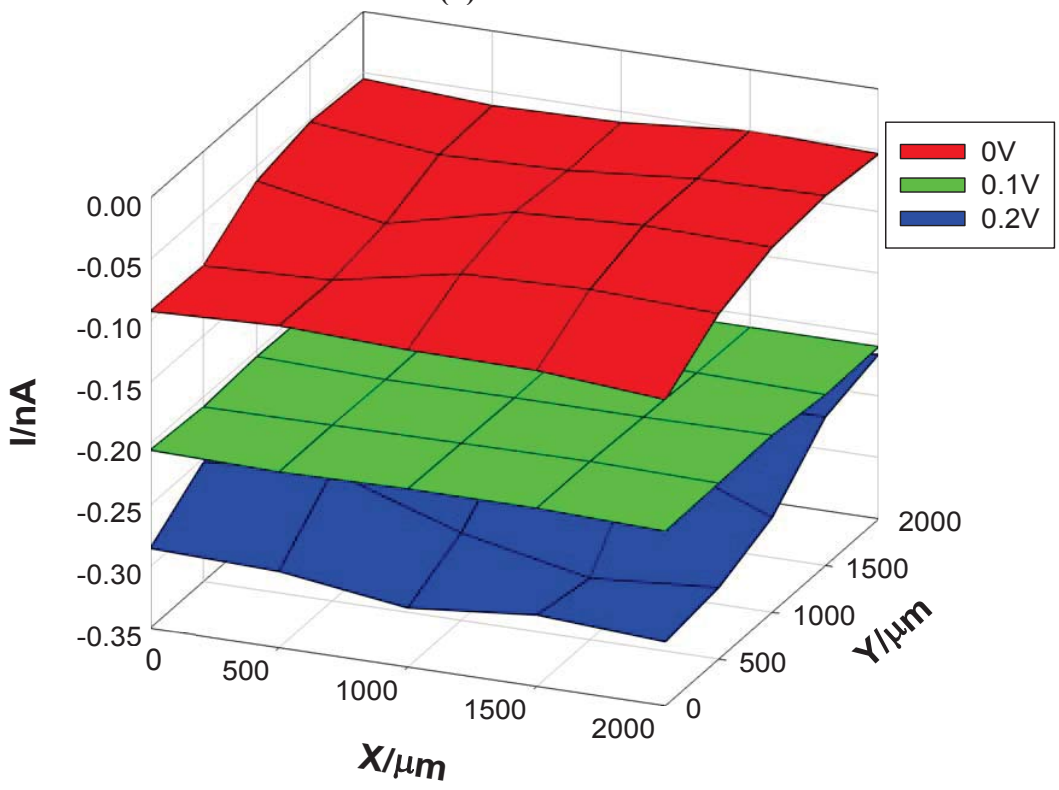

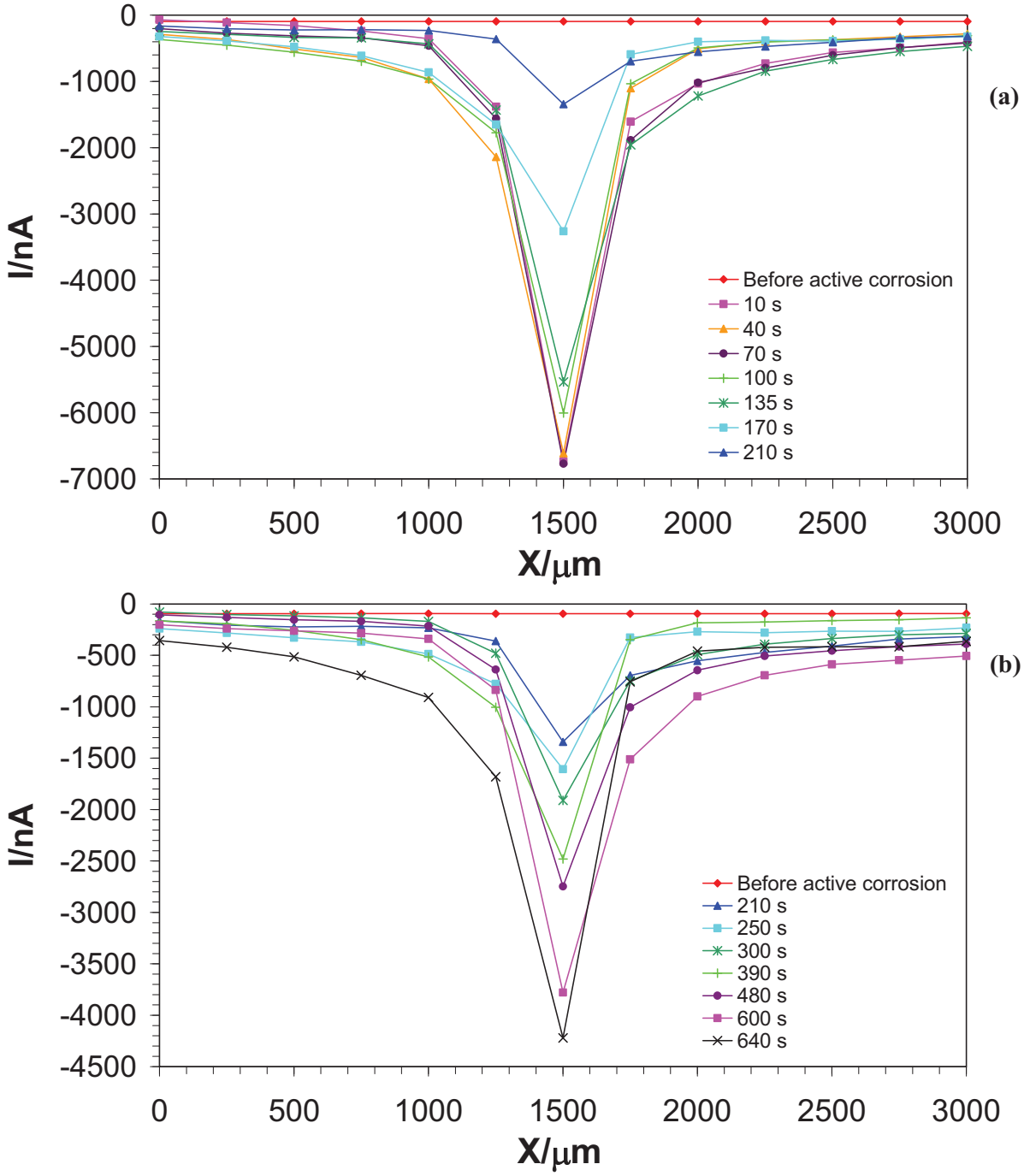
0
-1000
-2000
-3000
-4000
-5000
-6000
-7000
I/nA
0
500
1000
1500
2000
2500
3000
X/μm
Before active corrosion
10 s
40 s
70 s
100 s
135 s
170 s
210 s
(a)
0
-500
-1000
-1500
-2000
-2500
-3000
-3500
-4000
-4500
I/nA
0
500
1000
1500
2000
2500
3000
X/μm
Before active corrosion
210 s
250 s
300 s
390 s
480 s
600 s
640 s
(b)

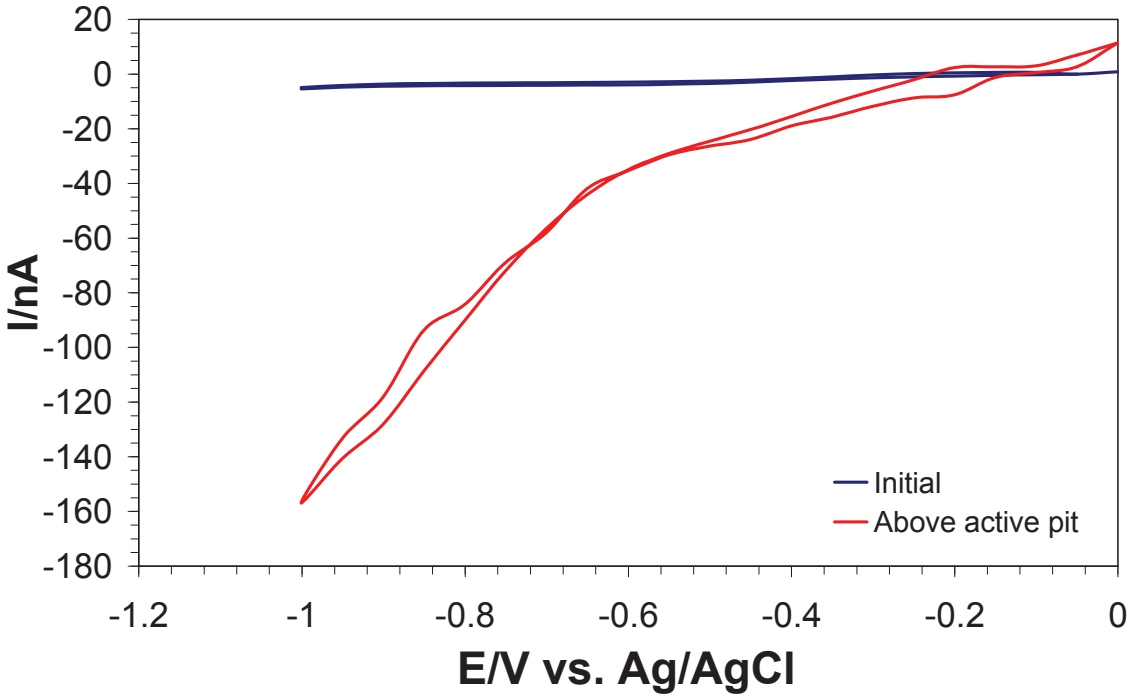
20
0
-20
-40
-60
-80
-100
-120
-140
-160
-180
I/nA
-1.2
-1
-0.8
-0.6
-0.4
-0.2
0
E/V vs. Ag/AgCl
Initial
Above active pit

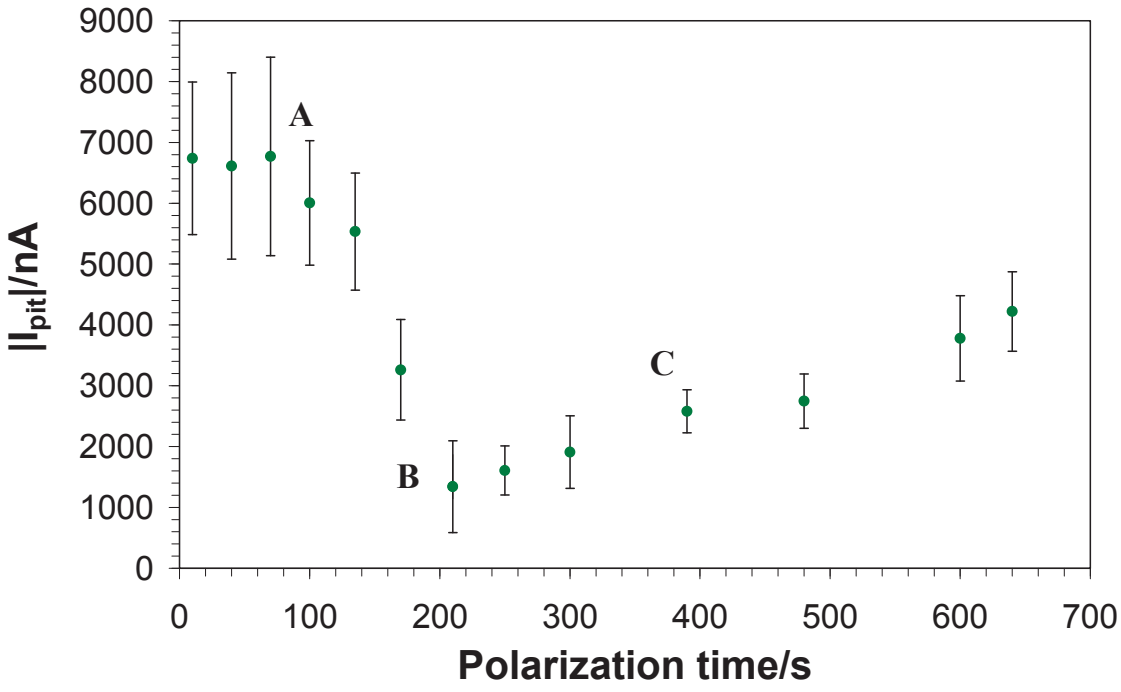
9000
8000
7000
6000
5000
4000
3000
2000
1000
0
|I_pit|/nA
A
B
C
0
100
200
300
400
500
600
700
Polarization time/s

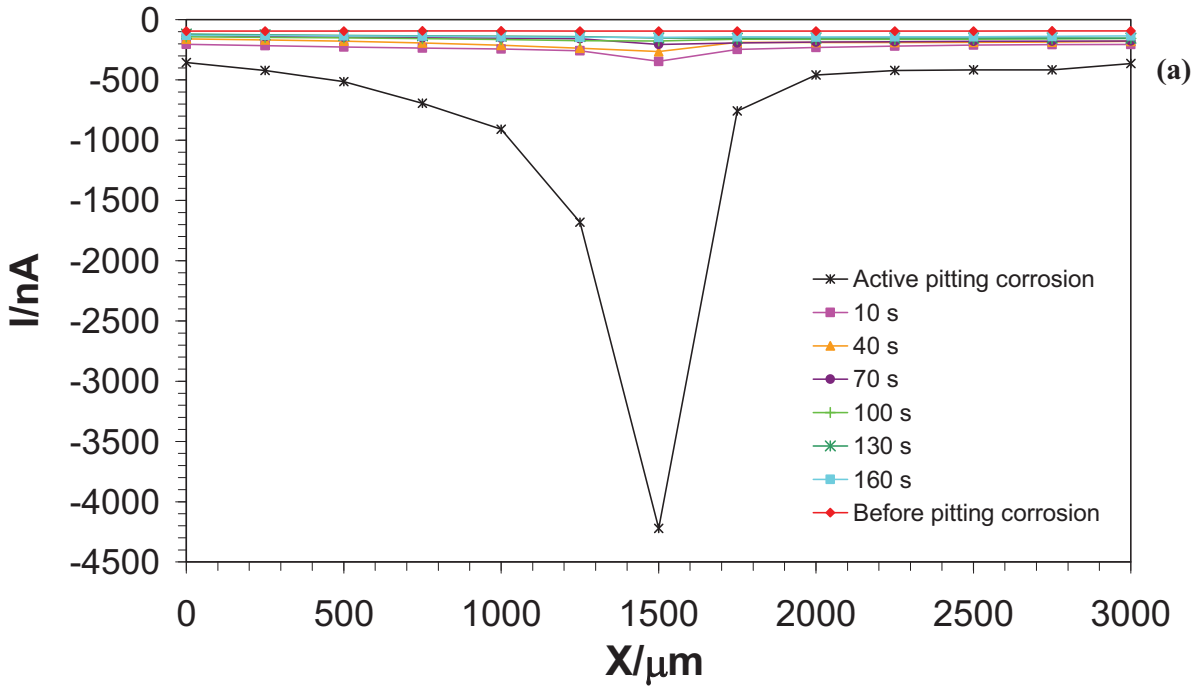
0
-500
-1000
-1500
-2000
-2500
-3000
-3500
-4000
-4500
I/nA
0
500
1000
1500
2000
2500
3000
X/μm
Active pitting corrosion
10 s
40 s
70 s
100 s
130 s
160 s
Before pitting corrosion

(a)

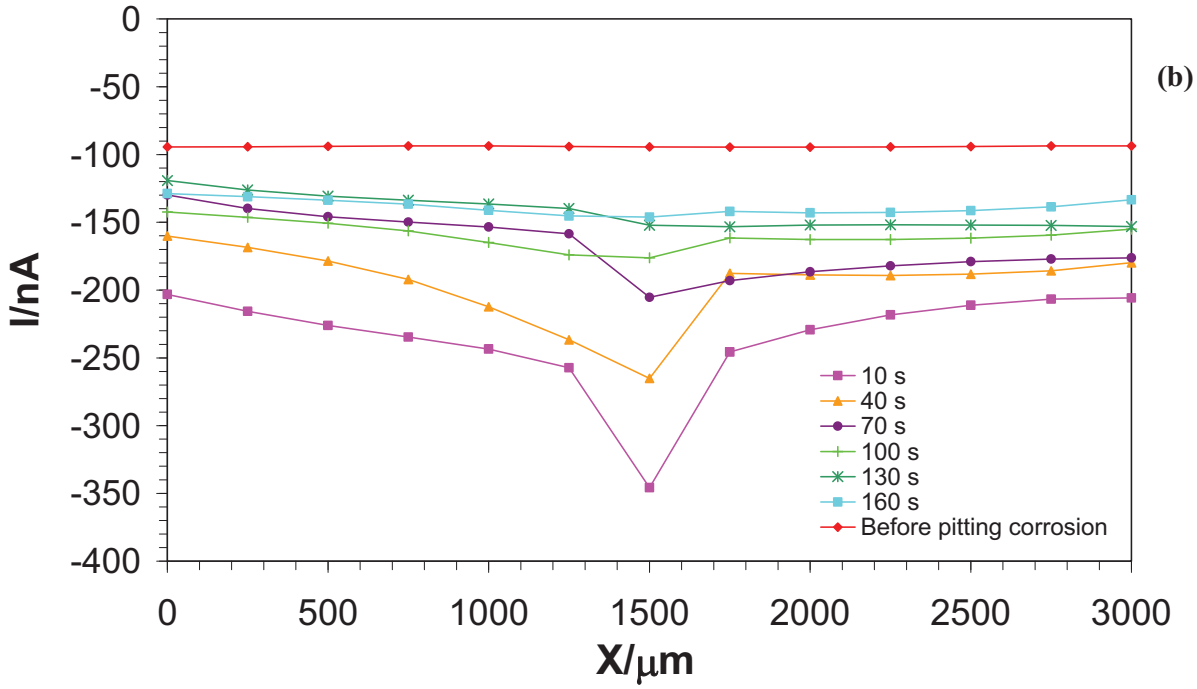
0
-50
-100
-150
-200
-250
-300
-350
-400
I/nA
0
500
1000
1500
2000
2500
3000
X/μm
10 s
40 s
70 s
100 s
130 s
160 s
Before pitting corrosion

(b)

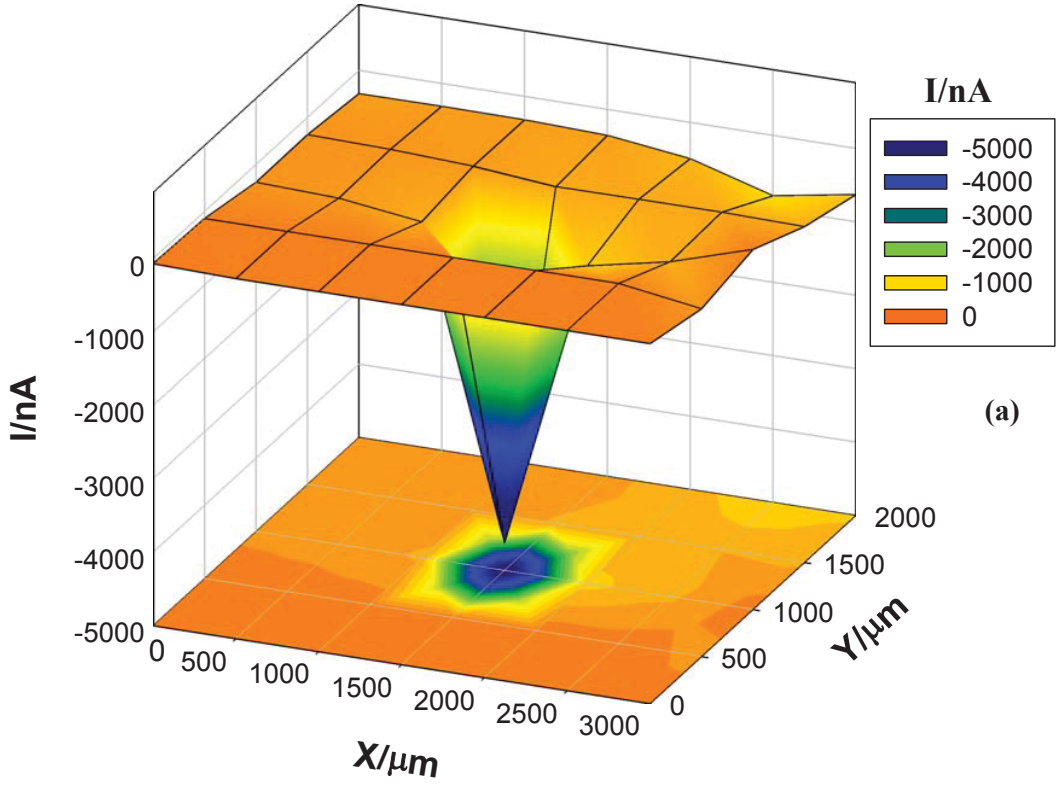
I/nA
-5000
-4000
-3000
-2000
-1000
0
I/nA
0
-1000
-2000
-3000
-4000
-5000
0
500
1000
1500
2000
2500
3000
X/μm
2000
1500
1000
500
0
Y/μm

(a)

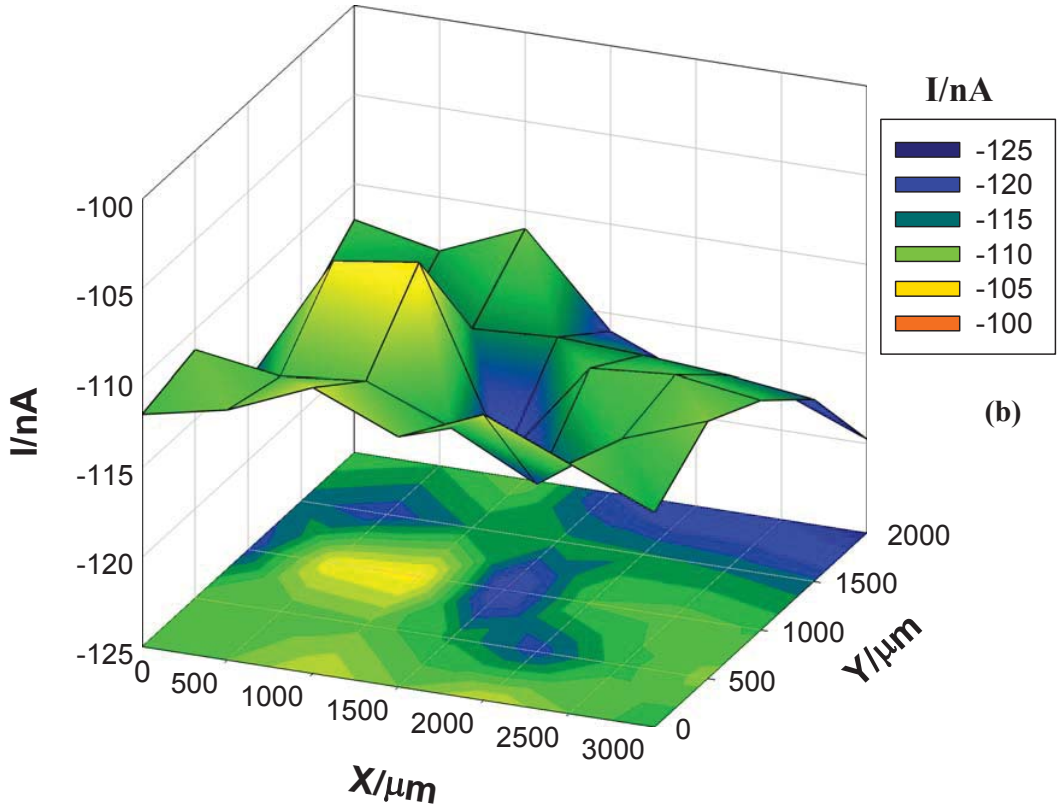
I/nA
-125
-120
-115
-110
-105
-100
I/nA
-100
-105
-110
-115
-120
-125
0
500
1000
1500
2000
2500
3000
X/μm
2000
1500
1000
500
0
Y/μm

(b)

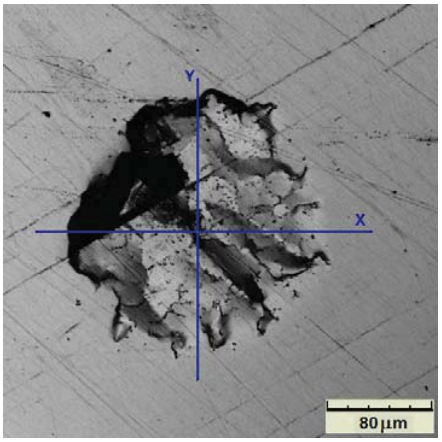
Y
X
80 µm

(a)

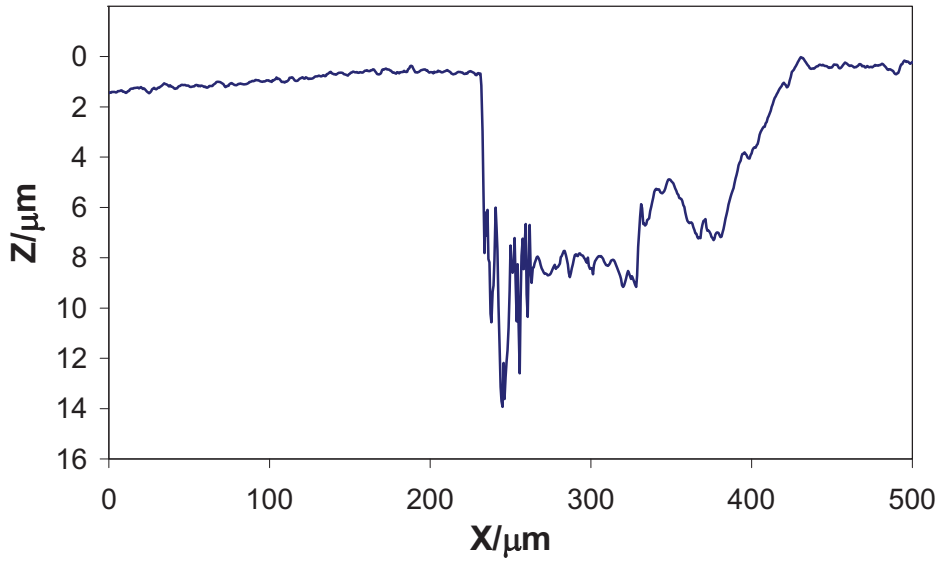
Z/µm
0
2
4
6
8
10
12
14
16
0
100
200
300
400
500
X/µm

(b)

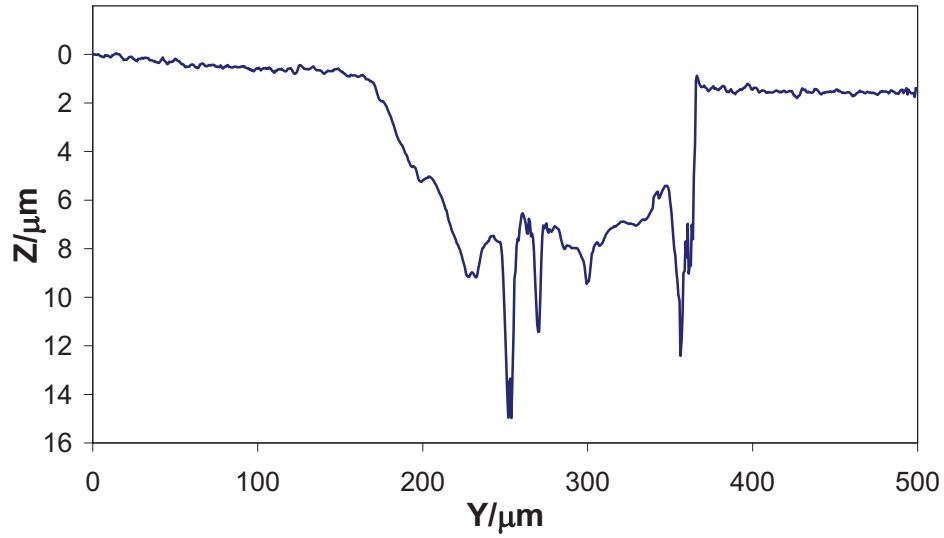
Z/µm
0
2
4
6
8
10
12
14
16
0
100
200
300
400
500
Y/µm

(c)